A numerical method for the solution of the three-dimensional acoustic wave equation in a marine environment considering complex sources

Giovanni Petris *, Marta Cianferra, Vincenzo Armenio

Dipartimento di Ingegneria e Architettura, Universitá di Trieste, Piazzale Europa 1, Trieste, Italy

ARTICLE INFO

Keywords:
Underwater acoustics
Wave Equation
FDTD
Complex Sources
Directivity

ABSTRACT

The need to understand how complex acoustic sources propagate noise in a realistic environment is of growing interest. In this work, we propose a numerical model for the simulation of noise generated by sources with directivity and propagating in ocean waveguides. The numerical model solves the wave equation for the acoustic pressure in the physical space using a second-order accurate finite difference method (FDTD). The source is implemented using an improved form of the hard-source method, which implicitly takes into consideration the reflection of acoustic waves associated to the presence of the ocean free surface, through the use of the method of images. This novel method is shown to improve the results with respect to the standard hard source implementation. We first validate the numerical method considering both analytical solutions and benchmark cases for the case of a monopole and then explore the acoustic energy patterns developed in the case of dipole and quadrupole sources. Specifically, the algorithm and the implementation of complex sources are evaluated first in a semi-infinite fluid layer and then considering two classical waveguides: the Ideal one and the Pekeris one. The comparison with analytical results shows the numerical method's accuracy and that incorporating free surface effects in the hard source implementation improves results. In addition, the study shows that the acoustic response in the near field, of the order of few kilometers from the source, is strongly influenced by the source's directivity and orientation relative to the free surface. The results of this paper have implications for future research aimed at characterizing and quantifying ship propeller noise in realistic waveguides. Indeed, this preliminary work is necessary to proceed to more complex numerical experiments, such as considering a real propeller signal as a source or considering stratification of the medium or propagation in confined domains such as experimental tanks.

1. Introduction

Characterization and prediction of propagation of anthropogenic noise at sea is a field of research of paramount importance because of the impact that it may produce on marine life. In 1982, the United Nations Convention on the Law of the Sea (UNCLOS) Anon (1982) recognized the hazard associated with the input of acoustic energy (noise) in the marine environment. More recently (2008), the European Union created a framework (Anon, 2008) to monitor and mitigate the anthropogenic impact on the marine environment, focusing, among the others, on underwater noise.

Noise at sea is due to the propagation of the acoustic pressure in the fluid. It is affected by seabed morphology, waveguide properties, and sediment rheology. Although the behavior of the acoustic energy in the three-dimensional (3D) space has been addressed in the past (Tolstoy, 1996), it still constitutes an undergoing field of research due to the complexity of the problem (Lin et al., 2019). Mathematical models have been developed over the latter decades for the prediction of the propagation of acoustic waves at sea. Most of them consider the interaction of omnidirectional sources with the environment. They do not examine the effects of the directivity of complex sources, which is ubiquitous of most anthropogenic sources, the latter being the cause of the majority of noise pollution in the ocean (Hildebrand, 2009).

Several acoustic propagation models have been proposed in literature to reproduce the underwater sound environment. Their choice depends on the acoustic problem under investigation (Etter, 2012). They are characterized by the range of frequency of the source, the variability of the domain with the distance from the source (range-dependent vs. range-independent), and by the source location (whether in a shallow or deep water environment).

When the solution is needed in the very far-field (order of ten-to-hundred kilometers along the horizontal directions), the best preferred choice consists in the solution of the Helmholtz equation, which

* Corresponding author.
E-mail address: petrisgiovanni@gmail.com (G. Petris).

https://doi.org/10.1016/j.oceaneng.2022.111459
Received 23 July 2021; Received in revised form 16 March 2022; Accepted 30 April 2022

represents the wave equation for the acoustic pressure recast in the frequency domain. The solution is obtained in a two-dimensional (2D) domain, so the acoustic pressure is evaluated over vertical slices of the ocean environment, namely a fluid waveguides bounded by a free surface above and by the seabed below. To reconstruct a three-dimensional (3D) environment $N\times 2D$ slices along the azimuthal direction should be considered unless fully 3D models are used. The comparison between these two approaches ($N\times 2D$ versus 3D) has been carried out by Sturm (2005) for the case of the propagation of a broadband acoustic pulse within an ocean canyon. The 3D approach was found to estimate a higher sound pressure level inside the canyon than the $N \times 2D$ approach highlighting the limitations of the latter. In Sturm (2005), the author used a Parabolic Equation (PE) model, which is often used for low-frequency sources in range-dependent environments both for shallow- and deep-water cases. For high frequencies sources, the ray theory model is the most reliable; the work of Weinberg (Weinberg and Keenan, 1996) highlights the capabilities of this theory in a shallow water domain. A serious limitation of the ray theory is the difficulty of reproducing complex directivity patterns, which can significantly impact the near-field acoustic response in a 3D environment. To be mentioned that the initial development of these models was oriented toward the analysis of the far-field noise, although in recent years the understanding of the impact of anthropogenic sources in the near field in shallow water situations is becoming of increasing importance.

Typical solutions of the Helmotz equation are obtained with omnidirectional sources, although most of the anthropogenic noise is characterized by a significant directivity. The propagation of the acoustic pressure originated by a point source with a complex directivity pattern in a fluid waveguide has been addressed in Haug et al. (1974), Kuznetsov and Stepanov (2007); more recently, the effects of vibrating source with specific directivity pattern on complex marine environments were analyzed in Zou et al. (2018, 2020), Jiang et al. (2018, 2020) regarding problems of fluid–structure interaction. Kuznetsov and Stepanov (2007, 2017, 2018) employed analytical approaches to evaluate the directivity of moving monopole, dipole, and quadrupole in a layered medium, thus considering the directivity of the source. Although not suited for the analysis of real complex sources, these latter methods can serve as a helpful benchmark for validation of numerical methods.

In recent years the available computational resources have led to the possibility to solve the wave equation directly in the time domain, using a discretization method, like, among the others, the finite-difference method. The finite-difference-time-domain (FDTD) method is suitable for relatively small domains and low-frequency sources and offers more flexibility on the shape and physical properties of the domain as well as on the properties of the source. Solving the Helmholtz equation in a 3D domain has a similar computational cost compared to solving the wave equation in the time domain, still being limited in the shape of the source. On the other hand, the solution of the wave equation in the physical domain is becoming more and more attractive for solving more complex problems. To be noted that the noise generated by a ship propeller (see, among the others Cianferra et al., 2019) has a significant low-frequency content and may impact the marine life in the surrounding field.

The solution in the physical domain enables considering the fluid inhomogeneity (namely variation of fluid density and speed of sound) and properties related to the solid matters layers present under the seabed; also, the direct solution of the wave equation, in principle, allows considering complex bathymetry. To be noted that the mentioned properties play an essential role in the propagation of sound because of the effects of refraction and reflection, which substantially modify the propagation pattern. Finally, sources more complex than the monopole, like dipole and quadrupole, and multiple moving sources can be directly considered. They are characterized by more elaborated directivity, which is relevant in the near field. It has to be pointed out that the solution in the 3D space is much more accurate than its 2D counterpart, in particular when analyzing the propagation in the near field and out of plane, which is affected by the non trivial reflection and refraction effects mentioned above. Finally, fully 3D solutions allow visualization of the whole acoustic field, enabling the observation of properties of the acoustic environment that are difficult to observe on a line or at specific microphones.

Preliminary work on the direct solution of the wave equation in the physical space was delivered by Fricke (1993). The author considered a two-dimensional axial symmetric domain, using the FDTD approach and focused on the scattering of Arctic ice, taking into consideration the elasticity of the medium. More recently, Hafla et al. (2018) studied noise generated by marine hydrokinetic power devices, solving the wave equation using the velocity–pressure system of equation by the adoption of the FDTD method in a three-dimensional space. The combination of the continuity equation, the momentum equation, and the equation of state leads to a system of partial differential equations, where both pressure and the velocity field have to be solved. This approach is suited for seismology purposes, for example, where velocity and acceleration are required to estimate the seismic hazard. However, in hydroacoustics, the primary variable of interest is pressure. As a consequence, from the above-mentioned system of PDEs (Bergmann, 1946) it is possible to derive the acoustic wave equation where the acoustic pressure is the only variable.

The acoustic wave equation is easier to implement and to be solved numerically compared to the velocity–pressure system of equations, retaining most of the advantages; the most important is the possibility to obtain a detailed map of the acoustic field in the space–time domain together with the possibility to implement complex sources in a three-dimensional space. On the other hand, some difficulties arise in implementing open boundary conditions and the attenuation properties of a medium. Regarding the implementation of the source, it is possible to take advantage of research in room acoustics, which is based on the FDTD method (Botteldooren, 1995), and it is of primary importance. To be noted that, compared to underwater acoustics, room acoustics studies the propagation of high frequencies in small domains, although the implementation is equivalent. We are interested in the low-frequency range, which is generally easier to solve in the physical domain. It is possible to use the *hard source* approach, where the pressure values generated by the source are supplied as a boundary condition within the computational domain.

The *hard source* technique allows to implement, within the 3D propagation model, the noise source obtained from a separate simulation (see, among the others (Cianferra et al., 2019; Cianferra and Armenio, 2021) for the characterization of the source at a laboratory scale and at a full scale) or from a campaign of experiments. To make the mathematical model more effective, considering that the marine environment is characterized by the presence of the free-surface (mathematically expressed by an homogeneous Dirichlet condition for the acoustic pressure), the *hard source* approach is herein expanded, taking into consideration the effect of the boundary in the evaluation of the source. The new strategy, which takes advantage of the method of images, is found to improve the results.

This is the strategy accomplished in the present paper, which represents the first step of a long-standing research project aimed at the development of a mathematical model for the simulation of the noise generated by a moving body at sea in the presence of the free surface and propagated in a real marine environment, characterized by the presence of stratification and complex bathymetry. To show the ability of the methodology to reproduce noise propagation in a 3D domain representative of the marine environment, we analyze the acoustic response of the Pekeris waveguide in the presence of three distinct sources: a monopole, a dipole, and a quadrupole. To analyze the property of the acoustic waveguide in the presence of complex sources, we quantify and visualize the acoustic energy distribution in the 3D domains, which constitutes a new achievement since most literature studies are conducted considering omnidirectional, monopole-like

sources. This because analyzing the acoustic pressure propagation of sources characterized by strong directivity is crucial to understanding how real sources (for example, hydrokinetic turbines or ship propellers) impact the marine environment.

Overall, the mathematical framework herein developed, from one side takes advantage of numerical methodologies well established in the literature, although commonly employed for other purposes, from the other side adapts these methodologies to the marine environment to build up a novel mathematical model for the analysis of noise generated by complex anthropogenic sources at sea and propagated in the near-to-intermediate field. Although the present paper reports the first step of the research, it contains significant outcomes: (i) a novel numerical method is developed for the marine environment and carefully validated with benchmark cases; (ii) an accurate three-dimensional analysis of the pressure field for extended domains is performed; (iii) it shows the effect of directivity of the source on the acoustic field propagated in the near-to-intermediate field.

First, we consider three different sources in a homogeneous domain limited by the presence of the free surface (the air–water interface), namely a monopole, dipole, and quadrupole, two over three of them exhibiting directivity in a semi-infinite fluid layer.

Successively we analyze the propagation of the monopole within two classical waveguides, the Ideal one and the Pekeris one, and compare our numerical results with standard analytical solutions.

Finally, since the directivity of a complex source is relevant for the propagation of the acoustic energy inside a fluid waveguide, we consider a dipole in two different geometrical configurations and a quadrupole within a Pekeris waveguide.

The paper is structured as follows. In Section 2, we describe the mathematical model and the numerical method, addressing the problem of source modeling. In Section 3, three different sources are utilized to validate the method considering propagation in a semi-infinite homogeneous space. In Section 4 we analyze propagation of a pressure signal within the ideal and Pekeris waveguides and compare results with analytical solutions; also Section 4 contains the analysis of propagation of signals generated by sources with increased complexity within the Pekeris waveguide. Section 5 contains concluding remarks.

2. The mathematical model

In this Section we first describe the mathematical model and, successively, we report the numerical implementation.

2.1. The acoustic wave equation

Acoustic signals are small perturbations of pressure originated by a source and propagated in a medium in form of waves. The pressure field p in a quiescent fluid can be written as

$$p = p_0 + p',$$

where p_0 is a bulk value (*i.e.* the hydrostatic pressure field) and p' a pressure perturbation. The pressure field can be associated to an equivalent density field

$$\rho = \rho_0 + \rho',$$

where ρ_0 is the bulk density giving rise to p_0, and ρ' is the density perturbation associated to p'. According to the linear wave equation, the perturbation propagates from a source point in the three-dimensional space. This equation is obtained by linearizing the mass and momentum conservation equations, assuming an inviscid fluid and adiabatic transformations. The three-dimensional wave equation for an inhomogeneous fluid reads as:

$$\frac{1}{c(\mathbf{x})^2}\frac{\partial^2 p'(\mathbf{x},t)}{\partial t^2} = \rho(\mathbf{x})\nabla\left(\frac{1}{\rho(\mathbf{x})}\nabla p'(\mathbf{x},t)\right) + S(\mathbf{x},t), \tag{1}$$

where c is the local speed of sound, $\mathbf{x}$ is the coordinate vector, t is time, and S is a source term. Hereafter, the symbol $(')$ is omitted for the sake of clarity.

Details and a rigorous derivation of the acoustic wave equation are in Pierce (2019). This modeling strategy is different from that associated with the Helmholtz equation and Hafla et al. (2018). The use of the wave equation in the physical space allows determining the space–time evolution of the acoustic disturbances in a general three-dimensional physical space. The main advantage of this approach is that one can consider a multi-directional source so as to study the directivity; likewise, it can consider a realistic (non-archetypal) propagation domain, which can produce diffraction and reflection of the acoustic waves. The fluid properties can vary along the three dimensions, overcoming the usual assumption of the idealized stratified medium.

All media are dissipative in nature, but since the focus of this work relies on the propagation of the pressure disturbance within the waveguide rather than on the interaction with the sediment layer, dissipation is not considered at this phase. The relation between stress and strain rules the absorption of energy by a medium; it depends on the medium's viscoelasticity and the frequency of the acoustic waves. Water exhibits a strong absorption in the range of high frequencies, above 1000 Hz, so it can be considered as a non-absorbing medium for low-frequency sources (Ainslie and McColm, 1998) and domains of the order of ten-to-hundred km. Several formulations of the acoustic wave equation that consider the attenuation have been introduced in literature, see, for example Petrov et al. (2012), where the evaluation of the propagation of the acoustic waves was performed over a 2D axial symmetric domain, which is a limiting feature in presence of complex sources. Attenuation will be considered in future research.

2.2. Numerical implementation

The partial differential Eq. (1) is here solved in a Cartesian $3D$-domain where the field variables are defined over the cell vertices. Eq. (1) is integrated using an explicit time-advancement scheme in conjunction with a centered in time and in space finite-difference algorithm. Overall, it is second-order accurate both in time and in space. For sake of clarity here we write down the discrete form of Eq. (1) in a one-dimensional space; the extension to the 3D case is straightforward.

$$\begin{aligned} p_i^n = {} & -p_i^{n-2} + 2p_i^{n-1} + \frac{\Delta t^2}{\Delta x^2} c_i^2 \rho_i * \\ & * \left[\frac{1}{2}\left(\frac{1}{\rho_{i+1}} + \frac{1}{\rho_i}\right)\left(p_{i+1}^{n-1} - p_i^{n-1}\right) - \frac{1}{2}\left(\frac{1}{\rho_i} + \frac{1}{\rho_{i-1}}\right)\left(p_i^{n-1} - p_{i-1}^{n-1}\right)\right] + \\ & + \frac{\Delta t^2 \rho_i c_i}{\Delta x}\left(\sigma_i \psi_{i+1}^{n-1} - \sigma_{i-1}\phi_{i-1}^{n-1}\right), \end{aligned} \tag{2}$$

where p_i^n is the acoustic pressure at the point defined by the index i at the iteration time n. The distance from the source in the x-direction is defined as $x = i\Delta x$, where Δx is the spacing between two consecutive vertices in the x-direction. The overall time of the simulation is $T = n\Delta t$, where Δt is the time interval. The indices $n-1$ and $n-2$ denote the two previous time steps, respectively. The density, (ρ_i), and speed of sound (c_i) of the ambient fluid are assigned at the cell vertices of the computational grid. In order to compute the Laplacian term, the density at the midpoints between two vertices is required. We calculate this density using the harmonic mean since it is better suited for the algorithm's stability in the presence of a sharp density gradient. We drop the source term S, since in the hard source implementation the source is treated as a boundary condition.

In Eq. (2) we see an additional term not present in Eq. (1), which contains two auxiliary variables ψ, ϕ and a damping coefficient σ. These variables arise from the Perfectly Matched Layer (PML) method,

described in Chern (2019). This method is used to avoid spurious reflection at the open boundaries. A wave without attenuation, apart from the geometrical spreading, is able to propagate to infinity, but the numerical domain must be limited. In absence of a reflective boundary that constrains the energy, the waves have to leave the numerical domain, making necessary the implementation of an open-boundary condition. For low-order schemes and 1-D problems, exact open-boundary conditions are available, which damp the wave's amplitude without reflecting energy inside the domain Engquist and Majda (1977). For 3-D problems, different types of open-boundary conditions were proposed in the literature to minimize spurious reflection inside the domain. Among them we implemented the PML method, which smooths the waves in a layer of cells close to the lateral boundaries of the computational domain. In this buffer layer (PML region) the modified wave Eq. (2) which contains the additional damping coefficient (σ), ensures that the pressure is correct at the first plane of computational points next to the region of the computational domain where the numerical solution is valid. Consequently, due to the properties of the modified wave equation, the error cannot propagate back into the domain, and the acoustic waves propagating in the PML layer are damped. The PML proposed by Chern (Chern, 2019) is exact, to machine zero, for homogeneous cases (where no jump in density occurs) and exhibits small reflection in the presence of density discontinuities.

The computational domain is split into two regions, the *real* one and the PML one. In the *real* region, the acoustic wave equation (Eq. (1)) is solved with the *damping coefficients* σ_i set to zero; in the PML region, the additional term must be evaluated using two additional evolution equations for each direction of propagation of the signal (Eq. (3)) for the variables ψ and ϕ. The two equations, in discrete form, read as:

$$\begin{cases} \phi_i^n = \phi_i^{n-1} - \frac{1}{2}\Delta t c_i \left(\sigma_{i-1}\phi_{i-1}^n + \sigma^n s_i \phi_i\right) - \frac{1}{2\Delta x}\left(p_{i+1}^{n-1} - p_{i-1}^{n-1}\right) \\ \psi_i^n = \psi_i^{n-1} - \frac{1}{2}\Delta t c_i \left(\sigma_{i-1}\psi_i + \sigma_i \psi_{i+1}\right) - \frac{1}{2\Delta x}\left(p_{i+1}^{n-1} - p_{i-1}^{n-1}\right). \end{cases} \tag{3}$$

The variables, which are defined at the cell vertices (i) of the numerical grid are used to decrease the acoustic pressure in the PML region, and are evaluated from the pressure field and can be initialized (at time step $n = 0$) as zero. In three dimensions, a total of six equations for the auxiliary variables are defined since two auxiliary variables are introduced for each direction. The *damping coefficients* is set to $\sigma_i = 1/\Delta x$ as suggested in Chern (2019). The only free parameters to be set are the PML thickness and the number of grid points where the *damping coefficients* σ_i is not zero. We found that imposing a thickness length proportional to the principal wavelength of the source is sufficient to obtain a satisfactory damping of the incoming waves together with negligible numerical reflections of the pressure waves over the boundary of the computational domain. Note that here the equations are solved in dimensional form in opposite to the non-dimensional one presented in Chern (2019).

The layout of the numerical method is as follows:

1. Initialization: The physical ($p_i^n, p_i^{n-1}, p_i^{n-2}$) and auxiliary ($\psi_i^n, \phi_i^n$, $\psi_i^{n-1}, \phi_i^{n-1}$) fields are initialized at zero. The field variables, ρ_i, c_i, are initialized so as to map the ocean environment, and σ_i is initialized as discussed above.
2. Time Loop: The following time loop is repetend n times until final time T is reached.
   - Acoustic Pressure: The value of p_i^n is evaluated from Eq. (2) at locations i of the numerical domain. Note that the 3D version of Eq. (2) has i, j, k indexes for space location, and the Laplacian term also contains the derivatives in the other two directions.
   - Source: The source term is imposed at the source location as a time-varying Dirichlet boundary condition, $p_i^n = p(x,t)_{analitycal}$, where the imposed values are evaluated from the know analytical function at the position $x = i\Delta X$ of the numerical grid and at the time $t = n\Delta T$.
   - PML: The value of ψ_i^n, ϕ_i^n are evaluated from Eq. (3). Note that in the 3D space, four additional equations are solved since four auxiliary variables are added, two for each direction. The methodology is explained in detail in Chern (2019).
   - Free-surface Boundary Condition: Pressure is set to be zero at the water/air interface so as to reproduce the complete reflection of acoustic waves.
   - Final Step: All the physical and auxiliary fields are updated, $p^{n-1} = p^n$, $p^{n-2} = p^{n-1}$, $\psi^{n-1} = \psi^n$, $\psi^{n-1} = \psi^n$
3. Data Collection: The dataset is stored for successive post-processing and analysis.

We are interested in reproducing the ocean waveguides; thus, we need to consider an inhomogeneous medium, with variations of density and speed of sound along the fluid column. Note that in our case, these two variables do not change in time, so the numerical domain's physical properties are steady. This is a very reasonable assumption since the time scale of acoustic wave propagation is much smaller than that of density variation along the fluid column.

The mathematical model herein considered evaluates the propagation in a fluid medium since the shear component of the velocity is not considered; this approach is exact for the water layer and it is approximated for a sediment layer. The interaction with the seafloor becomes relevant in a shallow water environment, so, as a consequence, the sediment layer needs to be modeled. It is often a good approximation to consider only compressional waves for the sediments since the shear wave speed is very low compared to that in solid rocks. This enables the evaluation of the acoustic wave propagation from the water layer to the sediment layer without solving for the shear wave.

The air–water interface is represented by a pressure-free boundary condition $p = 0$, reflecting the acoustic energy back into the domain. This is a good approximation since the transmission coefficient is almost zero due to the sharp gradient of density and speed of sound at the interface (Brekhovskikh et al., 1991). The boundary condition is applied as a Dirichlet boundary condition. The amplitude of the reflected waves is equal to the incident one, apart for a 180° phase shift.

The time step is constant in our simulations, and it is defined by the stability criterion of the numerical method. It is evaluated with the von Neumann criterion for the proposed numerical scheme $\Delta t \leq (1/c) * (1/dx^2 + 1/dy^2 + dz^2)^{-1/2}$. Note that the time step of the simulation decreases with cell size. The source frequency determines an upper limit for spatial discretization. Indeed, to resolve the wave propagation correctly, a minimum number of points is required for the reproduction of the smallest wavelength. For a second-order method, the minimum number of points required *per* wavelength is 8 (Dablain, 1986); this is the criterion adopted in our simulations.

The numerical method herein described is characterized by the presence of numerical dispersion. The consequence of the discretization of the wave equation is that the speed of sound of the discretized waves becomes a function of the grid spacing. As discussed in Dablain (1986) the computational domain has to be set in order to limit the numerical dispersion in relation to the problem dimension and frequency of the source. In presence of second-order methods, the dispersion error is such that higher frequencies tend to travel with a lower speed of sound. However, this problem is only alleviated by the available computational resources since increasing the number of computational nodes decreases the numerical errors.

2.3. Implementation of the source

Most studies on the acoustic source's characterization come from research in room acoustics (Bilbao and Hamilton, 2018; Sheaffer et al., 2014); the outcome of this research can be easily applied to underwater acoustic also in consideration of the fact that underwater sources are

easier to model since they operate in a low-frequency range, while most of the numerical errors are related to very high-frequency signals. Among the possible strategies of implementing the source, three are commonly in use, namely the *hard source*, the *soft source*, and the *transparent source*.

The *hard source* may be considered the simplest method. It consists of imposing the acoustic pressure at the source node(s), where Eq. (1) does not need to be solved, whereas the source function S is set to zero in the computational domain. However, several drawbacks are known to be related to this method. The first is related to the frequency; a phase delay is observed with increasing the frequency of the source. This problem is overcome by imposing the correct pressure in multiple clustered points (Bilbao and Hamilton, 2018). Other difficulties arise when the source is positioned near a wall. The hard source acts as a barrier, and all the energy incident to the source nodes is reflected away, generating extra pressure. Also, the hard source does not account for the reflection of the signal due to the presence of the wall. This issue will be discussed in the following.

The second method used in literature to implement the source is the *soft source*. The source function S is considered in the wave Eq. (1) and updated at the source nodes at each time step. This method allows avoiding the numerical errors of the hard source implementation because the incoming waves can pass through the source and interfere with it. The problem is that the pressure evaluated at the source location is not the prescribed one, in terms of intensity. The correct response of the source is obtained if the results are normalized, making not straightforward the use of this approach for real-world application. This method has additional limitations when considering finite size sources because, in this case, the acoustic pressure must be prescribed at all grid points, even if they are contained within the source, posing additional constraints to its use in real-world applications.

The *transparent source* was developed (Schneider et al., 1998) to eliminate the scattering property of the hard source, making the source transparent to incoming waves. The applicability of this method is limited to line source and point sources, making it not suited for multiple clustered points and, moreover, it requires high computational cost since two numerical simulations are required to obtain the solution.

Here we use the hard source method for its simplicity and because it is possible to define the value of pressure evaluated using analytical function exactly. Moreover, if the pressure of a more complex source is known at specific points, which coincides with the points of the numerical grid, the pressure from that points can be propagated into the numerical domain. This approach allows the direct computations of the propagation of noise from complex sources, which are not constructed from simple sources, such as a propeller, once its noise signature is known at specific points.

In Fig. 1 we show the nodes close to the source, the latter depicted in red. The analytical function representing the source is known, and it is used to evaluate the pressure at the gray nodes. The nodes are then considered as time varying boundary conditions and represent the acoustic pressure produces by the source. From these nodes, the acoustic pressure is propagated into the numerical domain. A better characterization of the source can also be achieved using the second-nearest neighbor points or the third-nearest ones, thus considering a larger box to impose the acoustic pressure.

In general, most methods for solving acoustic waves propagation do not consider the interference between the source and the incoming waves. In presence of a free surface in the propagation domain, the use of the image method can mitigate this problem. The effect of the reflected wave onto the source nodes can be evaluated and added to the source imposed pressure, as follows:

$$p_{hard\ img}(r,t) = \hat{p}_{hard}(r,t) + \hat{p}_{img}(r_{img},t)\mathcal{H}(t - r_{img}/c), \tag{4}$$

where $\hat{p}_{img}$ is the $\hat{p}_{hard}$ function evaluated at r_{img}, which is the distance between the source and its image. The Heaviside function acts as a delay activating the image source only upon the arrival of the first reflected wave. The advantage of considering an image source when adopting the hard source model in the presence of a free surface is here tested in the case of a monopole source and is discussed in the next Section 3.1. This method is defined as *hard img source*, in contrast with the classical *hard source*.

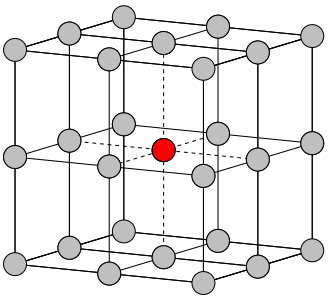

Fig. 1. Schematic of the hard source implementation. The red dot is the source and the gray dots represent the computational grid points where the pressure signal is imposed as boundary condition. (For interpretation of the references to color in this figure legend, the reader is referred to the web version of this article.)

3. Validation of the method

In this Section, we describe the results for the noise generated by three different sources, namely monopole, dipole, and quadrupole. These three sources are relevant for the underwater noise propagation problem because they, or a composition of them, represent archetypal models of real noise sources present at sea, like, among the others, ship propellers and hydrokinetic turbines. The dipole and the quadrupole exhibit directivity patterns and allow the evaluation of the directivity effect in a marine environment. In Fig. 2 we report a schematic of the sources used in the present paper.

In our numerical experiment, the marine environment is represented as a semi-infinite homogeneous water domain bounded by a top free surface. This simplification allows the use of the image method to obtain an analytical solution of the problem. An image source is placed by the opposite side with respect to the free surface so that the result inside the real domain is the sum of the acoustic pressure generated by the real source and by the image source. The sign of the image source is opposite to that of the real source so as to verify the condition $p = 0$ at the free surface (Rienstra and Hirschberg, 2004). Hereafter the speed of sound is $c = 1500\,\mathrm{m\,s^{-1}}$ and the water density is $\rho = 1000\,\mathrm{kg\,m^{-3}}$. The frequency of the source is set to f_{20} =20 Hz and f_{100} =100 Hz respectively giving wavelengths λ_{20} = 75 m and λ_{100} = 15 m, respectively. The wavelength associated to the source λ_f (f stands for the frequency of the source), is used to make the length non dimensional. Hereafter, the symbol $\tilde{(\cdot)}$ defines non dimensional quantities. As a consequence the grid spacing of 1 m gives $\tilde{\Delta x}_{20} = 0.013$ and $\tilde{\Delta x}_{100} = 0.066$ respectively for the two frequencies. The numerical domain is $600m$ ($8\lambda_{20}$ and $40\lambda_{100}$) long in the x-direction, $200m$ ($2.66\lambda_{20}$ and $13.33\lambda_{100}$) deep in the z-direction, and 100 m ($1.33\lambda_{20}$ and $6.66\lambda_{100}$) large in the y-direction. Open-boundary conditions are imposed over all directions but the top surface, in order to mimic a semi-infinite column of water bounded from above. The numerical grid satisfies requirement about the minimum number of points per wavelength, and the overall dimension of the domain is within the value suggested in Dablain (1986) to minimize the dispersion error.

The sound power radiated by these sources changes from case to case. At the same frequency, the quadrupole and dipole do not radiate the same energy as the monopole. Thus, the sound power radiated by the dipole and quadrupole is normalized with respect to the sound power radiated by a monopole in a uniform homogeneous domain. A careful derivation of the sound power radiated by the sources presented in the next Section, is described in (Norton and Karczub, 2003).

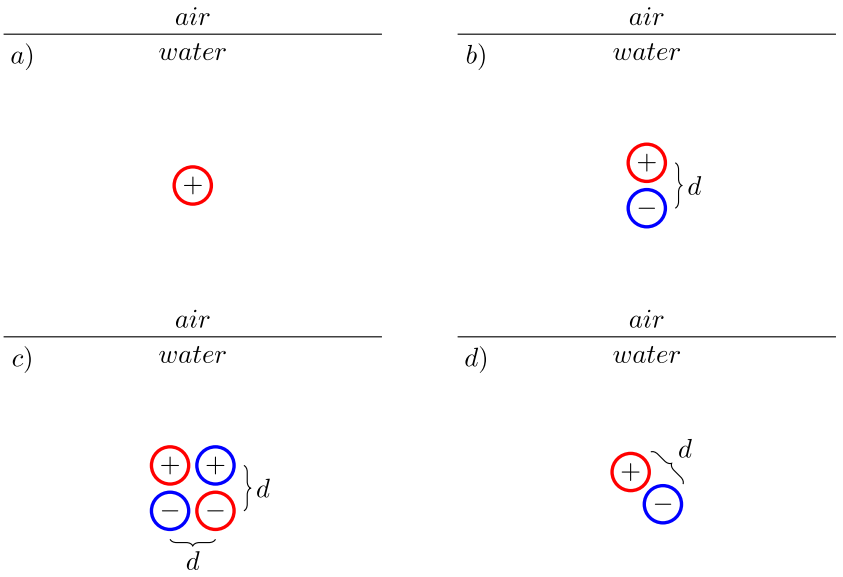

Fig. 2. Schematic of the sources used in this study: (*a*) monopole; (*b*) dipole; (*c*) quadrupole; (*d*) 45° inclined dipole.

3.1. Monopole

The monopole radiates the acoustic pressure with spherical symmetry, an assumption used in most underwater acoustic research to describe the sources. The acoustic pressure generated by a monopole $p_m(r,t)$ is:

$$p_m(r,t) = -\frac{ik\rho c Q_m}{4\pi r} e^{i(\omega t - kr)}, \tag{5}$$

where r is the distance from the origin of the monopole, t is time, Q_m is the source strength, $\omega = 2\pi f$ is the angular frequency, and $k = 2\pi/\lambda$ is the wavenumber. We remind the relation $c = \omega/k$, where c is the speed of sound in the medium. The associated sound power Π_m, in an infinite domain, is:

$$\Pi_m = \frac{Q_m^2 \rho c k^2}{8\pi}. \tag{6}$$

It is used as a reference quantity to normalize the source strength of the dipole and quadrupole, after imposing $Q_m = 1$.

The monopole source is located 36.5 m ($0.48\lambda_{20}$ and $2.4\lambda_{100}$) below the free surface at the center of the computational cell (Fig. 2a); it is used to estimate the error of our model, using the *hard source* and the *hard img source* method when comparing with the analytical solution. The free surface lies in the near field of the 20 Hz source and in the far-field for the 100 Hz one. In Fig. 3 we show the Sound Pressure Level (SPL) generated by the source on the $x-z$ plane passing through the source for both frequencies. The SPL is evaluated as follows:

$$SPL = 20\log_{10}\left(p_{rms}/p_0\right), \tag{7}$$

where p_{rms} is the root-mean-square of the pressure, and p_0 is the reference pressure, which for an underwater acoustic environment is $p_0 = 10^{-6}$ Pa. In Fig. 3 panel *a*, the 20 Hz source is in the near field, and significant interference pattern is not observed. In panel *b* of Fig. 3, for the 100 Hz source, the interference pattern is observed. It appears in the shape of divergent ribbons of pressure originated in the region between the source and the free surface. The interaction between the source and the free surface leads to the observation of minima and maxima of the SPL. This is known as the Lloyd Mirror effect (Tate and Spitzer, 1946). To be noted that, since the source has spherical symmetry, the solution is axial-symmetric as the planes of Fig. 3 are representative of the solution as a whole.

In Fig. 4, we show the comparison between the numerical results and the analytical solution; the pressure signal is sampled along the black line sketched in Fig. 3 at a depth of $z = 52m$. The numerical results are labeled Hard and Hard Img respectively based on the method used for the implementation of the source. For the 100 Hz monopole source a second numerical experiment is conducted with a refined grid, and the case is label Hard Refi, since the *hard source* method is used. In this case, the distance between two vertices is halved compared to the other cases in the three directions ($\Delta x_i = 0.5$ m$= 0.033\lambda_{100}$).

In Fig. 4 panel *a*, we observe a monotonic behavior for the SPL. The source and the free surface do not generate an interference pattern since the source is located on the near field of the free surface compared to the f_{100} monopole (Fig. 4 panel *c*), where a non-monotonic behavior is observed, reflecting the ribbon-like structure of the acoustic field.

In Fig. 4 panel *b* and *d* we show the relative error, which is evaluated as:

$$\text{Relative Error} = \frac{|SPL_{numerical} - SPL_{analitycal}|}{SPL_{analitycal}} \tag{8}$$

In the Hard case, the relative error increases with the distance from the source. Conversely, for the Hard Img case, we obtain better results. The relative error is almost constant along the line. For both cases the relative error is confined within 0.6%. The *hard img source* method gives better results because it directly takes in consideration the effect of the free surface on the source.

In Fig. 4 panel *d*, the relative error of the f_{100} monopole is higher than the f_{20} monopole. However, the maximum relative error of 15% is limited and confined where the SPL reaches the minimum. For the Hard and Hard Img cases the minimum value of the SPL is still correctly obtained, and, the error is mainly associated to a small shift of the curves due to a weak dispersion feature, and, away from the minima, the relative error is bounded below 4%.

The higher error of the f_{100} monopole is related to numerical dispersion, the dependency of the speed of sound on the frequency. Indeed, the numerical scheme herein employed is such that higher frequencies travel slower (Dablain, 1986). Consequently, the distance at which the minimum of SPL occurs for the numerical simulation is shorter than for the analytical solution. The refinement of the grid reduces the error associated with the numerical dispersion. The distance at which the minimum of the SPL occurs is evaluated correctly as observed for the Hard Refi case, and in this case the relative error is below 4% along the line.

To summarize, the *hard source* implementation corrected with the *hard img source* method is found to improve the results. However, it has to be noted that this method might fail under certain conditions

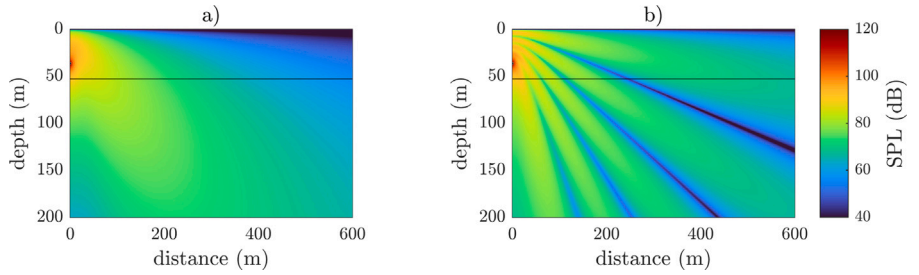

Fig. 3. SPL on the $x-z$ plane passing through the monopole source: (a) $f_{20} = 20$ Hz; (b) $f_{100} = 100$ Hz.

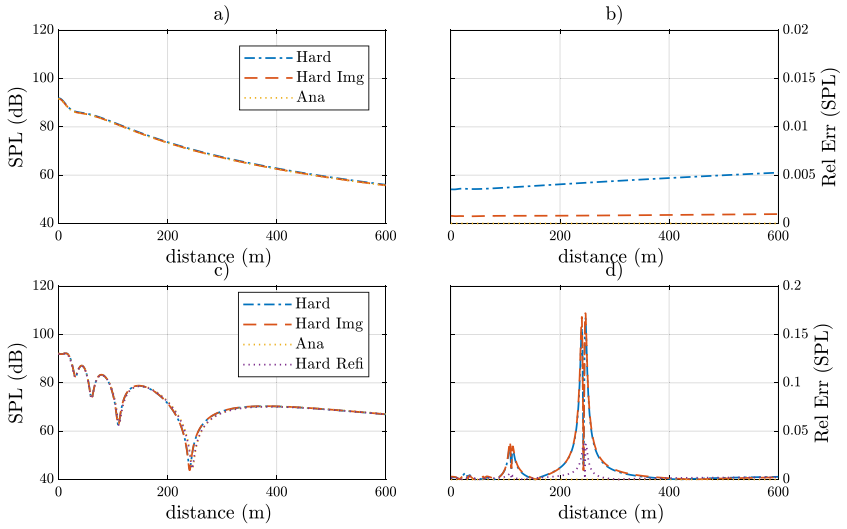

Fig. 4. Error analysis of the quadrupole source along a line at a depth of 52 m: (a) SPL of the 20 Hz source; (b) relative error of the 20 Hz source; (c) SPL of the 100 Hz source; (d) relative error of the 100 Hz source.

in the presence of density variation along the fluid column since the correction relies on the image method, which is based on the assumption of propagation in a semi-infinite homogeneous field. Specifically, the density and speed of sound variation along the fluid column are the main limiting factor. However, if this variation occurs at a distance larger than that of the source from the free surface the *hard img source* method still gives accurate results because the image solution implemented over the boundary nodes is not affected by inhomogeneities in the field.

3.2. Dipole

The second source herein considered is the dipole, characterized by two lobes and directivity. The dipole source $p_d(r,t)$ is made of two monopoles placed at a distance d from each other, and the dipole axis is parallel to the free surface (Fig. 2b). The acoustic pressure generated is:

$$p_d(r,t) = \frac{ik\rho c Q_d}{4\pi(r-d/2)} e^{i(\omega t - kr)} - \frac{ik\rho c Q_d}{4\pi(r+d/2)} e^{i(\omega t - kr)}, \tag{9}$$

where r is the distance from the origin of the dipole. The associated sound power Π_d, integrated over a sphere in an infinite domain, is the following:

$$\Pi_d = \frac{Q_d^2 \rho c k^4 (d/2)^2}{6\pi}. \tag{10}$$

Since k is usually $\ll 1$, the dipole is less efficient than the monopole in radiating energy. This is evident comparing the monopole and dipole sound power formula and assuming the same source strength. The source strength of the dipole Q_d is calculated setting its own sound power equal to that of a monopole with source strength $Q_m = 4\pi/\rho c k$, and d =0.4 m, obtaining the dipole source strength $Q_d \simeq 51.69\, Q_m$ for the 20 Hz source and $Q_d \simeq 10.34\, Q_m$ for the 100 Hz source respectively. The dipole source is placed at the same depth as in the previous cases (36.5 m), and the radiated pressure field is compared with the analytical solution.

In Fig. 5, we show the SPL of the source on the $x-z$ plane passing through the source. Panel a contains the SPL of the 20 Hz dipole. The space distribution of energy appears more complex than in the monopole case due to the directivity of the source. The SPL of the 100 Hz dipole shown in panel b is similar to the 100 Hz monopole, with a larger number of acoustic ribbons giving a larger number of planes of low pressure level. Also, the near field distribution of the acoustic pressure appears more complex than in the monopole case.

As for the previous case, we show the comparison between the numerical and the analytical results at a depth of 52 m (Fig. 6). In panel a we show the SPL profile of the 20 Hz dipole. The main difference observed compared to the monopole is the rapid decay near the source up to a local minimum. The relative error shown in panel b is limited to 2% for the Hard case, and it is maximum near the local minimum of SPL. The Hard Img case gives better results, and the relative error is almost constant across the domain and remains confined below the 0.5%.

In panel c, we show the SPL profile of the 100 Hz dipole. Compared to the monopole source, the amplitudes of the local minima are smaller, and these are clustered near the source. The dispersion error appears larger for the high frequency source, as shown in panel d. The relative error is limited within 3% for the Hard and Hard Img cases. The relative error of the Hard Img case is maximum at the second local minimum of the SPL profile, and then it remains nearly unchanged and below 1%. Conversely, the relative error in the Hard case increases with the distance from the source.

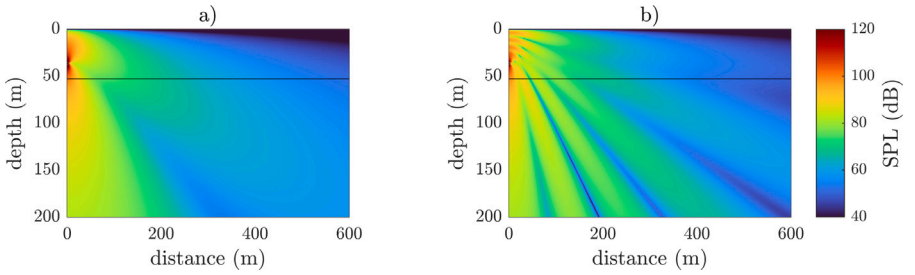

Fig. 5. SPL on the $x-z$ plane passing through the dipole source is shown. (a) $f_{20} = 20\,\text{Hz}$ source; (b) $f_{100} = 100\,\text{Hz}$ source.

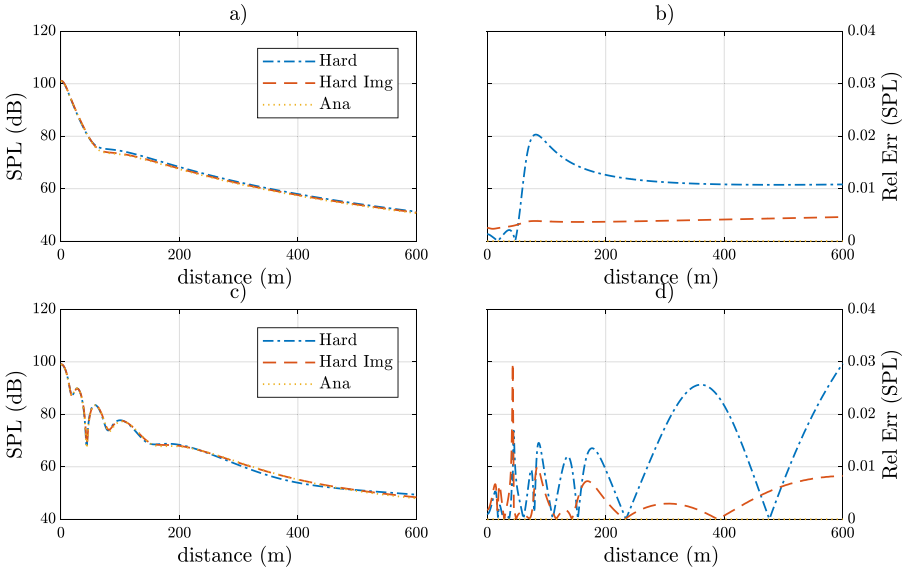

Fig. 6. Error analysis of the dipole source along a line at a depth of 52 m: (a) SPL of the 20 Hz source; (b) relative error of the 20 Hz source; (c) SPL of the 100 Hz source; (d) relative error of the 100 Hz source.

3.3. Quadrupole

The lateral quadrupole $p_q(r,t)$ is the latter archetypal source case herein studied. It is obtained from two dipoles (Eq. (9)) in opposition of phase placed at a distance d from each other, taking the distance d the same as in the dipole case (Fig. 2c). The associated sound power Π_q, integrated over a sphere in an infinite domain, is the following:

$$\Pi_q = \frac{4Q_q^2\rho c k^6 (d/2)^4}{30\pi}. \tag{11}$$

To obtain the same sound power of the previous case, keeping the monopole source strength to $Q_m = 4\pi/\rho c k$, the quadrupole source strength becomes $Q_q \simeq 3348.96 Q_m$ for the 20 Hz source and $Q_q \simeq 137.96\,Q_m$ for the 100 Hz source respectively. In Fig. 7 we show the SPL of the quadrupole source on the $x-z$ plane passing through the source. In panel a the SPL of 20 Hz quadrupole shows that the quadrupole introduces a plane of zero sound emission perpendicular to the free surface. For the 100 Hz quadrupole the distribution of the energy is similar to that of the other sources, namely in form of divergent ribbons propagating from the region confined between the source and the free surface.

The comparison between the numerical and the analytical solutions at a depth of 52 m is shown in Fig. 8. In panel a we show the SPL profile for the 20 Hz quadrupole. Compared to the dipole, we observe the presence of a minimum value of SPL in the near field. The relative error shown in panel b is smaller than 1.5% over the line for the Hard and the Hard Im cases. Increasing the frequency increases the number of local minima of the SPL (panel c). The relative error (panel d), does not increase significantly with the frequency. Overall, for the Hard and Hard Img cases, the error is smaller than 2%, and the latter gives better results near the source. As for the previous sources, the error is mostly associated with a slight spatial shift of the signal due to the mentioned dispersion error.

As a conclusion of Section 3, the analysis shows that the direct solution of the wave equation using an overall second-order accurate numerical scheme provides accurate results for a number of different sources, in a wide range of frequencies and for distances of the order of 40 λ, where λ is the wavelength of the source. The limiting factor for a second-order scheme is the minimum point per wave length required to solve the acoustic signal. Our results show that the dispersion error remains marginal at least up to 40 wave lengths, and it is expected to remain very small even for larger domains.

4. Acoustic propagations in waveguides

In the present Section we consider the propagation of an acoustic signal in two classical waveguides, the Ideal one and the Pekeris one, both representing a simplification of the marine environment. The two waveguides are standard benchmarks for the evaluation of the performance of propagation model. More benchmarks are described in Jensen and Ferla (1990). Most of them are relative to the propagation over long distances and are not of interest in the present work. In addition, these cases investigate the interaction between an omnidirectional source and a range-dependent environment, where the

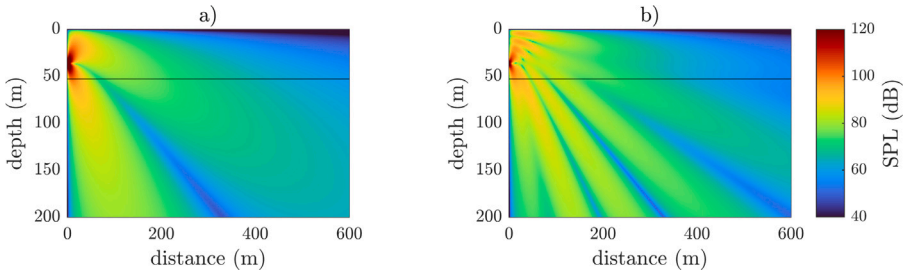

Fig. 7. SPL on the x-z plane passing through the quadrupole source. (a) the $f_{20} = 20\,\text{Hz}$ source; (b) the $f_{100} = 100\,\text{Hz}$ source.

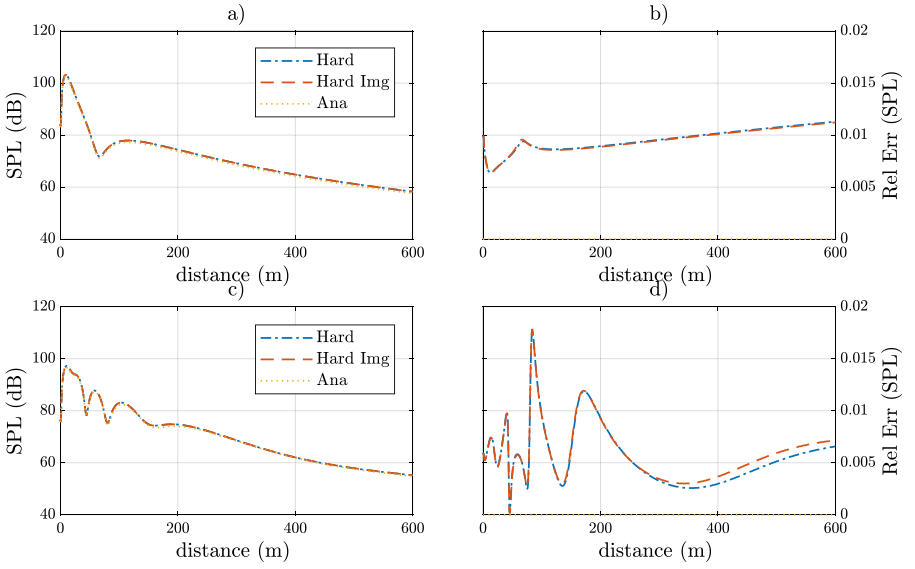

Fig. 8. Error analysis of the quadrupole source along a line at a depth of 52 m: (a) SPL of the 20 Hz source; (b) relative error of the 20 Hz source; (c) SPL of the 100 Hz source; (d) relative error of the 100 Hz source.

depth of the waveguide changes with the distance from the source; this is a topic of interest for future research. Further, we consider the acoustic response of the Pekeris waveguide considering the different sources discussed in the previous Section. Compared to the monopole's spherical symmetry, the introduction of a complex directivity pattern enables multiple configurations with respect to the free surface. An axis of zero sound emission characterizes the SPL generated by a dipole. This axis can be either aligned or inclined with respect to the free surface, generating a change of the acoustic energy distribution inside the waveguide. This aspect is considered in an additional case.

The first benchmark problem is the Ideal waveguide. The waveguide is range-independent, it extends at the infinite over the horizontal directions, and is bounded by two planes where the pressure is set to zero. The numerical domain used to reproduce the benchmark is shown in Fig. 9, panel a. The density of the fluid is $\rho = 1000\,\text{kg}\,\text{m}^{-3}$ and the speed of sound is $c_0 = 1500\,\text{m}\,\text{s}^{-1}$.

The second benchmark problem is the Pekeris waveguide. It is range-independent and extends at the infinite in the horizontal direction. Along the vertical, the homogeneous fluid layer is bounded from above by the free surface and below by an infinite layer of sediment. The numerical domain used to reproduce the benchmark is shown in Fig. 9, panel *b*. The density of the fluid is $\rho = 1000\,\text{kg}\,\text{m}^{-3}$ and the speed of sound is $c_0 = 1500\,\text{m}\,\text{s}^{-1}$. The sediment has a density of $\rho_{sediment} = 1800\,\text{kg}\,\text{m}^{-3}$ and the speed of sound is $c_{sediment} = 1800\,\text{m}\,\text{s}^{-1}$.

4.1. Ideal waveguide

A continuous 20 Hz monopole source is placed 36 m below the free surface in the Ideal waveguide (Fig. 9 *a*). The source function $p(t)$, imposed as *hard source* on a single node, is:

$$p(t) = \sqrt{2}\sin(2\pi f t), \tag{12}$$

where f is the frequency of the source, t is time, and $\sqrt{2}$ is an amplitude factor. The source is omnidirectional like the monopole, but with a finite amplitude at the origin. The pressure values used to obtain the results are collected in the time window $T - 3T$, where T is defined as the time needed by the acoustic pressure to reach the farthest computational boundary along an horizontal line. In the simulation, this distance is equal to L_x, and $T = L_x/c$, where c is the slowest speed of sound in the domain when different media are present. This approach is needed to allow the simulation to reach a statistically steady state. The numerical grid is uniform in all directions, and the grid cells dimension is 1 m, which normalized by the wavelength is 0.013; the largest horizontal extension of the numerical domain is 40 wave lengths. In Fig. 10 we show the numerical and the analytical results of the Transmission Loss (TL) of the monopole source in the ideal waveguide.

The TL, defined in Jensen et al. (2011), is:

$$TL(\boldsymbol{r}, \boldsymbol{r}_s) = -10\log_{10}\left(\frac{Z_0(\boldsymbol{r}_s)}{Z(\boldsymbol{r}, \boldsymbol{r}_s)}\left|\frac{p(\boldsymbol{r}, \boldsymbol{r}_s)}{p_0(\boldsymbol{r}_s)}\right|^2\right), \tag{13}$$

where $\boldsymbol{r}$ is the distance from the source, $Z(\boldsymbol{r}) = \rho(\boldsymbol{r})c(\boldsymbol{r})$ is the acoustic impedance of the medium, and p is the acoustic pressure. The TL is obtained by dividing the acoustic pressure at a distance $\boldsymbol{r}$ by a reference pressure given by the same source at reference distance $\boldsymbol{r}_s = 1$ m in a ho-

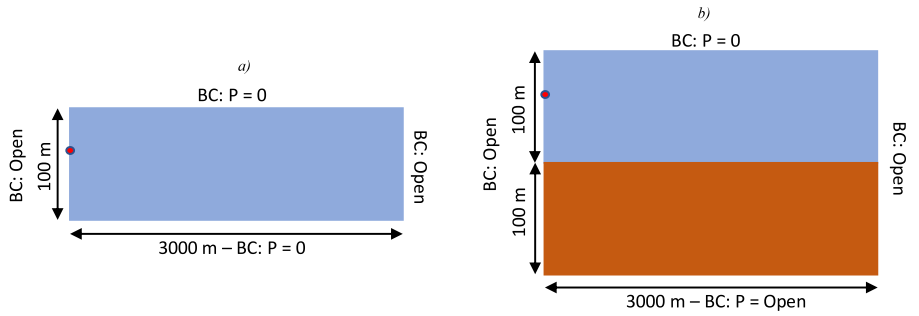

Fig. 9. Schematic of the waveguides: (a) Ideal waveguide; (b) Pekeris waveguide.

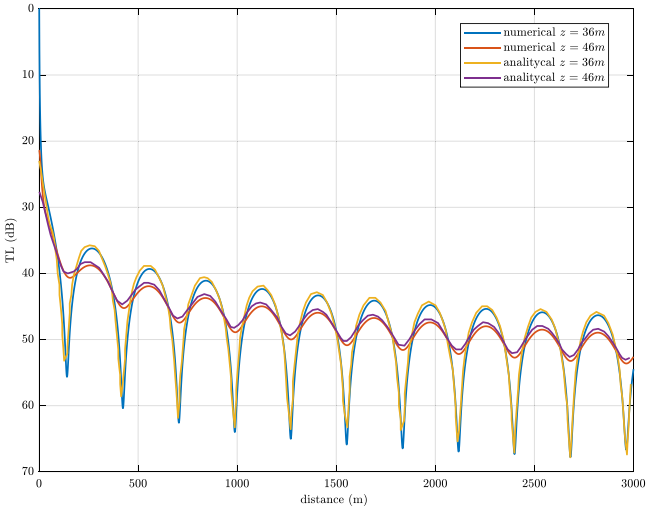

Fig. 10. Transmission loss for a 20 Hz continuous point source placed at 36 m of depth in the Ideal waveguide. The numerical and analytical results at $z = 36$ m and at $z = 46$ m.

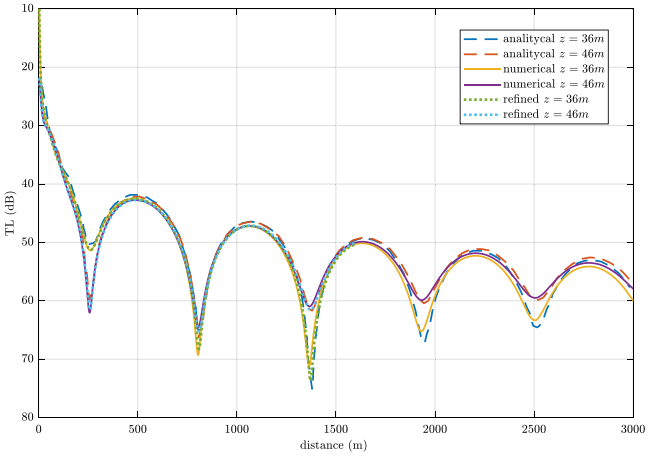

Fig. 11. TL for a 20 Hz continuous point source placed at 36 m depth in the Pekeris waveguide. Comparison between numerical and analytical results at $z = 36$ m and at $z = 46$ m.

mogeneous infinite medium. In our numerical experiment the acoustic pressure is evaluated in the time domain, as a consequence, $p(\boldsymbol{r}, t)$ is a function of time. For this reason in Eq. (13) the root-mean-square pressure p_{rms} is used instead of $p(\boldsymbol{r}, \boldsymbol{r}_s)$.

The analytical results are taken directly from Figure 2.23 panel *b* of Jensen et al. (2011), where the authors solved the Helmholtz equation, using the normal-modes approach.

The results are shown at two different depths, namely at the source depth 36 m and below, at 46 m. The characteristic oscillations of the TL, which are related to the two modes propagating in the waveguide, are well-replicated at both depths. These two modes have a specific modal interference length L_i, which in this case is of $L_i \simeq 300$ m, namely $6\lambda_{20}$. The difference in the amplitude of oscillation is related to the amplitude associated with the propagating modes, as explained in more detail in Jensen et al. (2011). At 36 m both modes are excited with the same amplitudes, and at 46 m the amplitude of the first mode is higher than that of the second mode. A spherical decay ($\sim 1/r$) is observed near the source. At a distance equal to the depth of the domain, as expected, we observe a cylindrical decay ($\sim 1/\sqrt{r}$). There is a 1 dB to 2 dB difference at the maxima of the two TLs. However, the difference is constant across the domain so that the error might be related to the method used to extract the reference data. The difference observed at the minima is basically due to the low resolution of the analytical results, as extracted by the reference paper. Overall, the second-order numerical method implemented for the solution of the wave equation in the physical space provides accurate results.

4.2. Pekeris waveguide

The second classical problem is the Pekeris waveguide, an archetypal representation of a shallow-water marine environment (Fig. 9b). The only physical boundary of the problem is the upper free surface, but the interface between the water and sediment layers entraps part of the acoustic energy inside the fluid waveguide and allows the propagation of the acoustic waves over long distances as in a real shallow water environment.

A 20 Hz monopole source is placed 36 m below the free surface and it is implemented as in the previous case using the function (Eq. (12)). The pressure values are collected in the time window $T - 3T$ following the previous approach. The numerical grid is uniform in all directions, and the grid cell dimension is 1 m, as in the previous case. In Fig. 11 we show the numerical and the analytical results of the TL of the monopole source in the Pekeris waveguide. As in the previous case, the analytical results are taken directly from Figure 2.29 panel *b* (Jensen et al., 2011). The authors obtained the analytical results solving the Helmholtz equation using a wavenumber integration approach. The results are shown at the source depth 36 m and at 46 m. The fact that the domain is a semi-infinite layer allows the energy to leave the domain by the bottom side, propagating in the sediment layer. As a consequence, the modal interference length is different compared to the Ideal waveguide case. In this case, it is larger, and it decreases with the distance from the source. Moreover, as discussed in Jensen et al. (2011), just two modes are excited, a lossless mode, which propagates without losing energy, apart the geometrical decay, and a leaky one, which losses energy with the distance. The difference in the magnitude

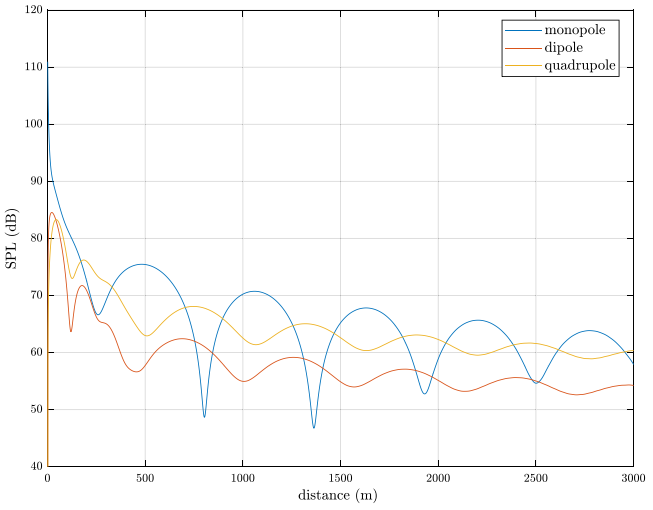

Fig. 12. SPL comparison at a depth of $z = 36\,\mathrm{m}$ between a 20 Hz continuous monopole, dipole, and quadrupole source in a Pekeris waveguide.

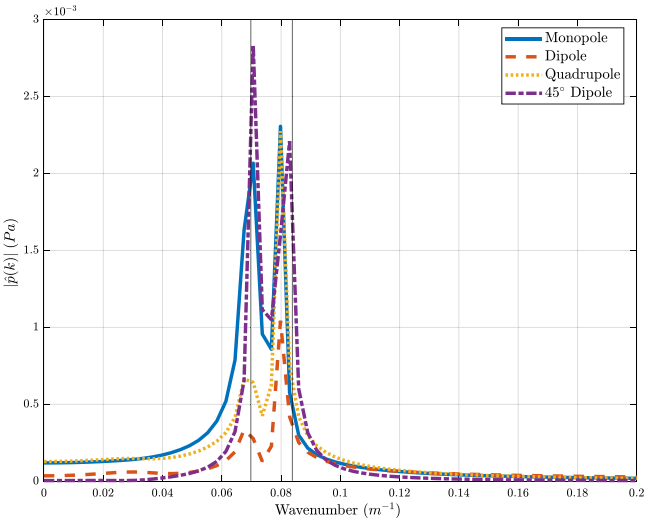

Fig. 13. Pressure amplitude $\hat{p}(k)$ of the Fourier Transform of the pressure field along the x-direction from 300 m to 2348 m at a depth $z = 36\,\mathrm{m}$ for the four sources considered in the Pekeris waveguide. The two vertical lines correspond to $k = \omega/c_{sediment}$ and $k = \omega/c_{water}$.

of the TL between the two depths is related to the amplitude at which the modes are excited. Compared to the Ideal waveguide case, the TL is larger for the Pekeris waveguide, since the energy is not constrained inside the fluid waveguide.

The comparison of the numerical and analytical results (Fig. 11) shows a difference of the order of 1 dB away from the minima of the TL. The maximum of the error is observed near the minima of the TL. This is comparable with the error observed in Fig. 4 panel (d), for the monopole with a higher frequency. The error is related to the numerical dispersion, which is known to increase with the frequency and, as observed in this case, with the distance from the source. Increasing the resolution of the numerical simulation reduces the error as shown in Fig. 4, where the refined grid is used (note that for the Pekeris waveguide we evaluated a refined-grid case also).

In the refined-grid case, the propagation of the source is evaluated on a smaller numerical domain, which is halved with respect to the standard domain, due to computational resource limitations. The grid cells dimension in the refined case is 0.5 m, which normalized by the wavelength is 0.0066. In the refined case, the error is reduced, in that the minima and maxima of the analytical solution are better reproduced. Up to the second minimum, the two numerical simulations give similar results. On the third minimum, the refined solution follows better the behavior of the analytical solution, although the results obtained with the coarse grid still appear of good quality.

The overall behavior of the interference pattern and the range of value of the TL is correctly reproduced by the numerical simulation. The errors can be reduced by implementing a higher-order method as in Hafla et al. (2018) although the second-order scheme herein presented produces accurate results.

4.3. Directivity signature on a Pekeris waveguide

The Pekeris waveguide (Fig. 9b) is used to evaluate the propagation of the three different sources described in Section 3. The physical characteristics of the waveguide and the numerical domain are the same as in the previous case, together with the duration in time of the simulation and the grid size. The sources have a frequency of 20 Hz and are placed at a depth of 36 m. The source strength has been chosen as described in Section 3. The different sources generate the same amount of energy as the monopole, although distributed with a specific directivity in space.

In Fig. 12 the SPL of the monopole, the dipole, and the quadrupole in a Pekeris waveguide are displayed at a depth of 36 m along a line along the x-direction. The increasing complexity of the dipole and quadrupole sources contributes to significant difference in the SPL profile in the vicinity of the source up to a distance of 500 m ($6.66\,\lambda_{20}$) where multiple local minima of the SPL are observed for the dipole and quadrupole cases compared to the monopole.

At a distance larger than 500 m ($6.66\,\lambda_{20}$), the characteristic oscillatory pattern and the cylindrical decay of the SPL are recovered. The SPL amplitude of the oscillations of the monopole is about 2.5 times larger than those of the dipole and quadrupole. Among the three sources, the dipole has the lower level of SPL across the domain; it is about 4 dB lower than that of the quadrupole and about 8 dB lower than that of the monopole.

The modal interference length is the same for the three sources, but it appears shifted by half the interference length for the quadrupole and less than half the distance for the dipole. This effect is related to the excitation of the modes inside the waveguide, which are the same described in the previous case. The amplitude at which the modes are excited depends on the source's depth and the type. As observed, the monopole at a depth of 36 m excites both modes with similar amplitude. Conversely, at the same depth the dipole and quadrupole excite the first (lossless) mode more than the second (leaking) mode as shown in Fig. 13. (details on these aspects are in the book of Jensen et al. (2011).)

The difference in the SPL is a direct consequence of the directivity. Only the monopole can propagate the same energy in every $x - z$ plane passing through the source, in opposition to the dipole and quadrupole sources.

In Fig. 14 we show the SPL over the vertical $x - z$ plane passing through the source. The presence of the sediment layer substantially changes the energy distribution inside the fluid waveguide, compared to the case discussed in Section 3. The typical Lloyd pattern is not observable in this case. The monopole (Fig. 14a) is able to better transmit energy inside the fluid waveguide compared to the other two sources. The dipole (Fig. 14b) transmits most of energy in the direction perpendicular to the free surface; consequently, most of the energy leaves the fluid domain, entering the sediment layer. The presence of a zero plane of sound emission perpendicular to the free surface for the quadrupole source (Fig. 14c) constrains energy over a specific

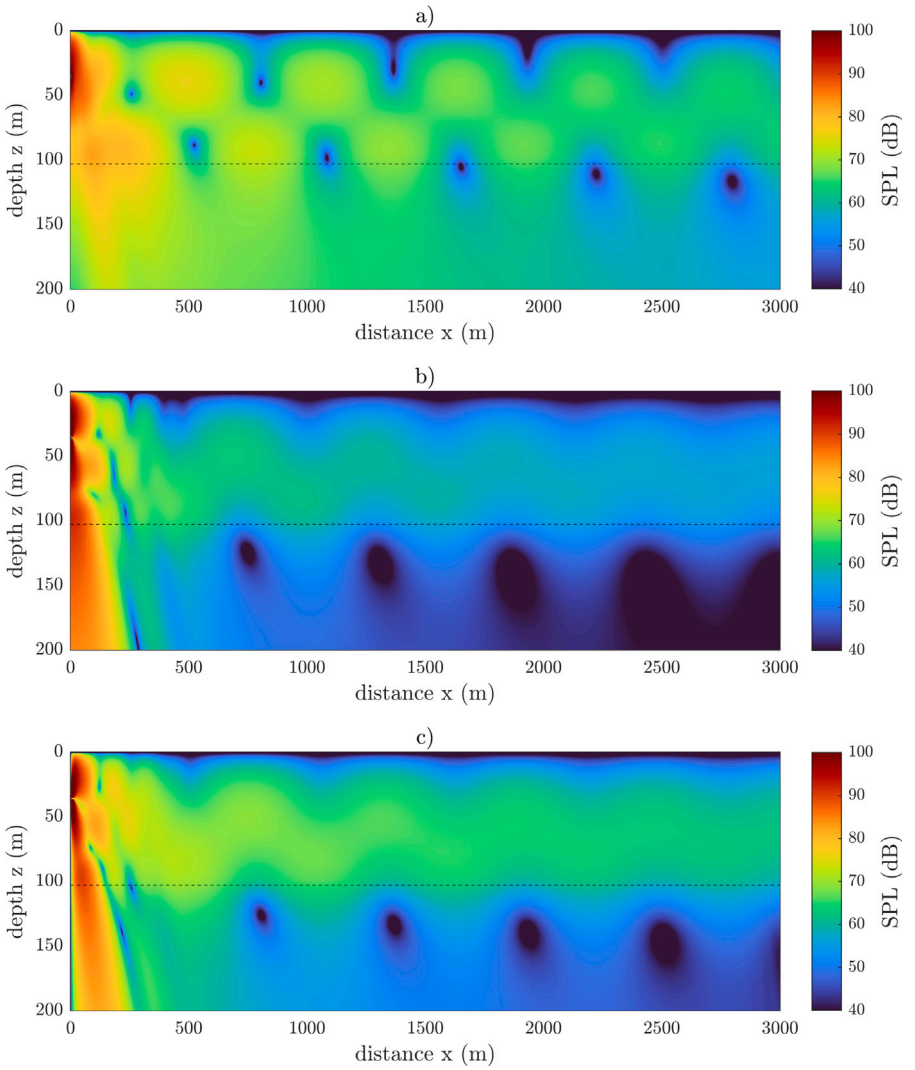

Fig. 14. SPL over the vertical $x-z$ plane at a depth of $z=36\,\mathrm{m}$: (a) 20 Hz monopole; (b) dipole; (c) quadrupole.

directions, and, as a consequence, more energy is propagated inside the fluid waveguide, compared to the dipole case.

The dipole maintains an axial-symmetry over the x-y plane, as shown in Fig. 15 panel (*b*). Along this plane, the distribution of energy is similar to the monopole (Fig. 15a). The quadrupole breaks the spherical symmetry over the x–y plane, as shown in Fig. 15, panel *c*. Only a quadrant of the x–y plane is shown due to the symmetry properties of the solution. The $y-z$ plane passing through the source, which is not shown, is identical for the monopole and dipole sources due to symmetry. The zero plane of the quadrupole is on the $y-z$ direction (Fig. 14 panel *c*) and it is not shown.

The monopole source, or, in general, the spherical symmetric source, is the typical type of source used to investigate the acoustic response of a marine environment due to its simplicity. The behavior of a more complex source far from the origin is somewhat similar to a monopole and, at a first approximation, it can be used as a reference. However, the SPL can be significantly different. Also, our results show that the monopole-like approximation is not valid in the near field, when the analysis of sound generated by complex sources is required.

4.3.1. Effect of inclination of the source on the propagation within a Pekeris waveguide

Finally, we consider the same Pekeris waveguide (Fig. 9b) used in the previous cases to evaluate the propagation of the acoustic pressure generated by the same dipole of the previous Section but inclined by 45° degrees with respect to the free surface (Fig. 2d). The main aim is to analyze the effect of a variation of the geometrical configuration of the source which exhibits a directivity on the noise propagated in the medium. We compare the results of this additional case study with those of the horizontal dipole discussed in the previous Section. The inclined dipole is placed at a depth of 36 m as the horizontal one. The physical characteristics of the waveguide and the numerical domain are the same as in the previous case, together with the time of the simulation and the grid dimension. In Fig. 16 we show the SPL level over an horizontal line at a depth of 36 m. The SPL is significantly affected by the inclination of the source. In the near field, up to a distance of 500 m ($6.66\,\lambda_{20}$), the decay of the signal is substantially different between the two cases. Specifically, the inclined dipole resembles the monopole, with a decay typical of a source exhibiting radial symmetry along this plane. (compare Fig. 16 with Fig. 12) Further, at intermediate distances (larger than 500 m, $6.66\,\lambda_{20}$) the signals appear different in shape and amplitude. The inclined dipole SPL profile resembles that of the monopole (compare Fig. 12). Specifically, the amplitude of the oscillations of the SPL is nearly doubled with respect to that of the horizontal dipole and more similar to that of the monopole. This is due to the fact that the orientation of the source may dramatically affect the amplitudes at which the modes are excited. In particular in Figure figure:wavenumber we show that the modes of the inclined dipole are

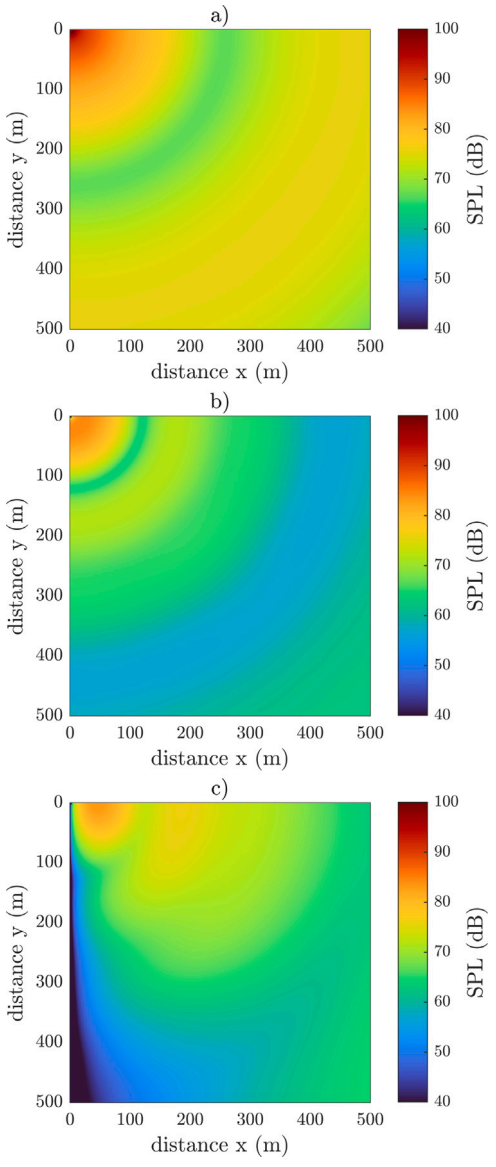

Fig. 15. SPL on a quadrant of the x–y plane at a depth of $z = 36$ m; (a) 20 Hz monopole; (b) dipole; (c) quadrupole.

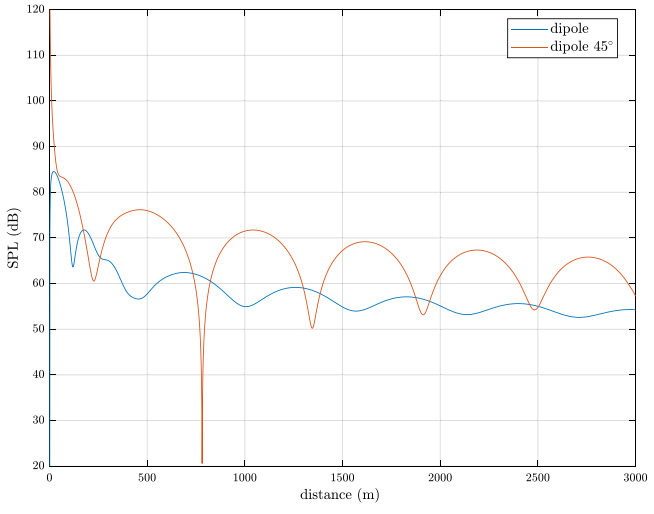

Fig. 16. SPL of the 20 Hz dipole at a depth of $z = 36$ m: (a) horizontal dipole; (b) dipole inclined by 45° with respect to the free surface.

comparable to those of the monopole. In Fig. 17 we show the SPL over the $x - z$ plane passing through the inclined dipole. The black line is at a depth of 100 m at the interface between the fluid layer and the sediment layer. The inclination of the dipole enables more reflection of energy at the seabed than the case of the horizontal dipole (Fig. 14b), where most of energy leaves the domain. This aspect is related to the angle of incidence of the acoustic waves at the interface between the two media. Obviously, different orientations may give rise to different energy patterns, showing that directivity typical of real world sources introduces non trivial effects worth of analysis. The minima of SPL along the water–air interface are narrower for the inclined dipole compared to the horizontal one. Different orientations may give rise to different energy patterns, showing that directivity typical of real world sources introduces non trivial effects worth of analysis. The situation may be even more complex in presence of multiple sources. This is a topic of a successive study.

5. Conclusion

In this paper, we presented the first important step of a long-standing research project aimed at quantifying the noise generated by anthropogenic activity at sea and propagated in a realistic inhomogeneous environment. We solve the acoustic wave equation ruling the propagation of acoustic pressure in ocean waveguides in the physical space using a standard finite difference time domain (FDTD) method. The numerical method is accurate at the second-order in time and space. The algorithm has been complemented with perfectly matched layer (PML) open boundary conditions aimed at minimizing the spurious reflection of acoustic waves occurring at the open boundaries of the domain. An improved version of the hard source technique has been developed to consider the presence of a complex noise source within the computational domain. In particular, as in the standard hard source method, the acoustic signal generated by the source is set as a boundary condition at grid points surrounding the source itself; In addition, we complement the technique considering the image method to reproduce the effect of the ocean free-surface on the reflection of the acoustic waves within the interior of the ocean. This improvement reduces unwanted spurious reflections, which appear when the source is placed near the free surface. The numerical method has been tested in a variety of cases. First, an extensive comparison between analytical and numerical solutions has been conducted for archetypal sources (monopole, dipole, quadrupole) with different frequencies in a semi-infinite homogeneous water domain. The method was found to reproduce the pressure signals accurately, provided that some resolution requirements are satisfied, particularly regarding the number of grid cells per wavelength. The implementation of the hard image source method was found to improve the results in all cases examined. Successively, two classical problems have been considered: propagation of the acoustic signals in the Ideal waveguide and the Pekeris waveguide. In both cases, the numerical model performed well; the dispersion error, associated with the second-order scheme employed for the spatial discretization, appeared of minor importance. The principal analysis carried out in the present paper regards the directivity, which is ubiquitous of most real-world noise sources in the ocean. However, our study shows that using a spherically symmetric source (*i.e.* monopole) is not sufficient to correctly characterize real sources in the near field since the energy distribution in the fluid waveguide is strongly affected by the type of source and the environment. In particular, the paper shows that the directivity modifies the way the fundamental modes are excited, and this reflects on the patterns of propagation of the acoustic energy in the ocean.

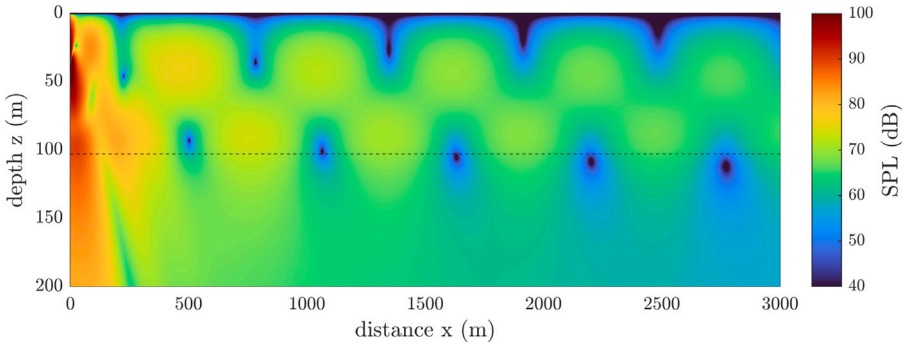

Fig. 17. SPL on the $x-z$ plane passing through the 20 Hz dipole inclined by 45° with respect to the free surface.

CRediT authorship contribution statement

Giovanni Petris: Conceptualization, Methodology, Software, Writing – original draft. **Marta Cianferra:** Conceptualization, Supervision, Writing – review & editing. **Vincenzo Armenio:** Supervision, Writing – review & editing.

Declaration of competing interest

The authors declare that they have no known competing financial interests or personal relationships that could have appeared to influence the work reported in this paper.

Acknowledgments

The present research has been developed within the Ph.D. Program Earth Science, Fluid-Dynamics, and Mathematics (ESFM) and was supported by OGS, Italy and CINECA, Italy under HPC-TRES program award number 2019–05.

References

Ainslie, M.A., McColm, J.G., 1998. A simplified formula for viscous and chemical absorption in sea water. J. Acoust. Soc. Am. 103 (3), 1671–1672.

Anon, 1982. 1833 UNTS 397, 21 ILM 1261. United Nations Convention on the Law of the Sea.

Anon, 2008. Directive 2008/56/EC of the European parliament and of the council of 17 2008 establishing a framework for community action in the field of marine environmental policy (Marine Strategy Framework Directive) (OJ L 164, 25.6.2008, 19–40).

Bergmann, P.G., 1946. The wave equation in a medium with a variable index of refraction. J. Acoust. Soc. Am. 17 (4), 329–333.

Bilbao, S., Hamilton, B., 2018. Directional sources in wave-based acoustic simulation. IEEE/ACM Trans. Audio Speech Lang. Process. 27 (2), 415–428.

Botteldooren, D., 1995. Finite difference time-domain simulation of low-frequency room acoustic problems. J. Acoust. Soc. Am. 98 (6), 3302–3308.

Brekhovskikh, L.M., Lysanov, Y.P., Beyer, R.T., 1991. Fundamentals of ocean acoustics.

Chern, A., 2019. A reflectionless discrete perfectly matched layer. J. Comput. Phys. 381, 91–109.

Cianferra, M., Armenio, V., 2021. Scaling properties of the Ffowcs-Williams and Hawkings equation for complex acoustic source close to a free surface. J. Fluid Mech. 927.

Cianferra, M., Petronio, A., Armenio, V., 2019. Non-linear noise from a ship propeller in open sea condition. Ocean Eng. 191, 106474.

Dablain, M.A., 1986. The application of high-order differencing to the scalar wave equation. Geophysics 51 (1), 54–66.

Engquist, B., Majda, A., 1977. Absorbing boundary conditions for numerical simulation of waves. Proc. Natl. Acad. Sci. 74 (5), 1765–1766.

Etter, P.C., 2012. Advanced applications for underwater acoustic modeling. Adv. Acoust. Vib. 2012.

Fricke, J.R., 1993. Acoustic scattering from elemental arctic ice features: Numerical modeling results. J. Acoust. Soc. Am. 93 (4), 1784–1796.

Hafla, E., Johnson, E., Johnson, C.N., Preston, L., Aldridge, D., Roberts, J.D., 2018. Modeling underwater noise propagation from marine hydrokinetic power devices through a time-domain, velocity-pressure solution. J. Acoust. Soc. Am. 143 (6), 3242–3253.

Haug, A., Graves, R.D., Uberall, H., 1974. Norma-mode theory of underwater sound propagation from directional multipole sources. J. Acoust. Soc. Am. 56 (2), 387–391.

Hildebrand, J.A., 2009. Anthropogenic and natural sources of ambient noise in the ocean. Mar. Ecol. Prog. Ser. 395, 5–20, Vancouver.

Jensen, F.B., Ferla, C.M., 1990. Numerical solutions of range-dependent benchmark problems in ocean acoustics. J. Acoust. Soc. Am. 87 (4), 1499–1510, Vancouver.

Jensen, F.B., Kuperman, W.A., Porter, M.B., Schmidt, H., 2011. Computational Ocean Acoustics. Springer Science & Business Media, Vancouver.

Jiang, L., Zou, M., Huang, H., Feng, X., 2018. Integrated calculation method of acoustic radiation and propagation for floating bodies in shallow water. J. Acoust. Soc. Am. 143 (5), EL430–EL436.

Jiang, L.W., Zou, M.S., Liu, S.X., Huang, H., 2020. Calculation method of acoustic radiation for floating bodies in shallow sea considering complex ocean acoustic environments. J. Sound Vib. 476, 115330.

Kuznetsov, G.N., Stepanov, A.N., 2007. The field of an equivalent multipole composite radiator in a waveguide. Acoust. Phys. 53 (3), 326–334.

Kuznetsov, G.N., Stepanov, A.N., 2017. Approximate analytic representations of laws of attenuation in vector-scalar fields of multipole sources in a pekeris waveguide. Acoust. Phys. 63 (6), 660–672, Vancouver.

Kuznetsov, G.N., Stepanov, A.N., 2018. Attenuation regularities of vector-scalar fields of multipole sources in Interference Maxima Regions. Phys. Wave Phenomena 26 (4), 334–341, Vancouver.

Lin, Y.T., Porter, M.B., Sturm, F., Isakson, M.J., Chiu, C.S., 2019. Introduction to the special issue on three-dimensional underwater acoustics. J. Acoust. Soc. Am. 146 (3), 1855–1857.

Norton, M.P., Karczub, D.G., 2003. Fundamentals of Noise and Vibration Analysis for Engineers. Cambridge University Press.

Petrov, P.S., Zakharenko, A.D., Trofimov, M.Y., 2012. The wave equation with viscoelastic attenuation and its application in problems of shallow-sea acoustics. Acoust. Phys. 58 (6), 700–707.

Pierce, A.D., 2019. Acoustics: An Introduction to its Physical Principles and Applications. Springer.

Rienstra, S.W., Hirschberg, A., 2004. An Introduction to Acoustics, vol. 18. Eindhoven University of Technology, p. 19.

Schneider, J.B., Wagner, C.L., Broschat, S.L., 1998. Implementation of transparent sources embedded in acoustic finite-difference time-domain grids. J. Acoust. Soc. Am. 103 (1), 136–142.

Sheaffer, J., Walstijn, M.van., Fazenda, B., 2014. Physical and numerical constraints in source modeling for finite difference simulation of room acoustics. J. Acoust. Soc. Am. 135 (1), 251–261.

Sturm, F., 2005. Numerical study of broadband sound pulse propagation in three-dimensional oceanic waveguides. J. Acoust. Soc. Am. 117 (3), 1058–1079.

Tate, J.T., Spitzer, L.J., 1946. Physics of Sound in the Sea: Summary Technical Report of Division 6. US. Government Printing Office, Washington DC, p. 566.

Tolstoy, A., 1996. 3-D propagation issues and models. J. Comput. Acoust. 4 (03), 243–271.

Weinberg, H., Keenan, R.E., 1996. Gaussian ray bundles for modeling high-frequency propagation loss under shallow-water conditions. J. Acoust. Soc. Am. 100 (3), 1421–1431.

Zou, M.S., Liu, S.X., Jiang, L.W., Huang, H., 2020. A mixed analytical-numerical method for the acoustic radiation of a spherical double shell in the ocean-acoustic environment. Ocean Eng. 199, 107040.

Zou, M.S., Wu, Y.S., Liu, S.X., 2018. A three-dimensional sono-elastic method of ships in finite depth water with experimental validation. Ocean Eng. 164, 238–247.